

Simulation of a strong steady-state plasma shock in a warm dense matter regime

Cite as: Phys. Plasmas **30**, 012706 (2023); <https://doi.org/10.1063/5.0129941>

Submitted: 07 October 2022 • Accepted: 21 December 2022 • Published Online: 18 January 2023

 Brett D. Keenan,  Chrismond D. Smith,  Daniel Livescu, et al.

COLLECTIONS

 This paper was selected as an Editor's Pick



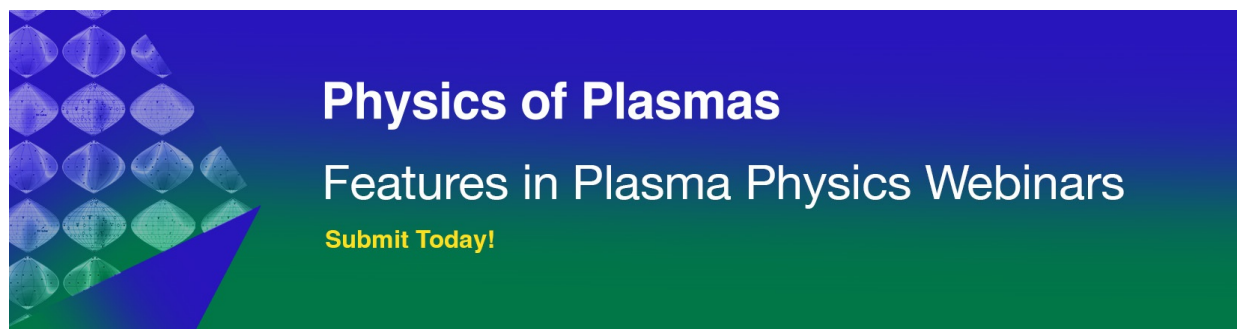
[View Online](#)



[Export Citation](#)



[CrossMark](#)



Physics of Plasmas
Features in Plasma Physics Webinars
[Submit Today!](#)

Simulation of a strong steady-state plasma shock in a warm dense matter regime

Cite as: Phys. Plasmas **30**, 012706 (2023); doi: [10.1063/5.0129941](https://doi.org/10.1063/5.0129941)

Submitted: 7 October 2022 · Accepted: 21 December 2022 ·

Published Online: 18 January 2023



View Online



Export Citation



CrossMark

Brett D. Keenan,^{1,a)}  Chrismond D. Smith,²  Daniel Livescu,¹  Jeffrey Haack,¹  and Robert S. Pavel¹ 

AFFILIATIONS

¹Los Alamos National Laboratory, Los Alamos, New Mexico 87545, USA

²University of Texas at San Antonio—One UTSA Circle, San Antonio, Texas 78249, USA

^{a)}Author to whom correspondence should be addressed: keenan@lanl.gov

ABSTRACT

The structure of collisional plasma shocks has been subject to an extensive, multi-decadal investigation—in the hydrodynamic, hybrid kinetic ion/electron fluid, and fully kinetic ion/electron limits. Despite this thoroughness, all of these studies apply exclusively to classical, weakly coupled plasmas. Here, we report the first results for a planar hydrodynamic simulation of a strong, steady-state shock in a subspace of the warm dense matter (WDM) regime. Specifically, we consider a plasma of fully degenerate electrons with moderate-to-strongly coupled ions. Since the WDM ion and electron transport coefficients and equation of state differ markedly from their non-degenerate, weak-coupling equivalents, we find that the structure of a WDM plasma shock notably deviates from the ideal plasma picture.

Published under an exclusive license by AIP Publishing. <https://doi.org/10.1063/5.0129941>

I. INTRODUCTION

The warm dense matter (WDM) regime covers a very broad range of material densities and temperatures and is quite ubiquitous in high-energy-density (HED) environments. Such settings where WDM may be found include white dwarf stars, the interior cores of the solar system gas giants, and certain phases of an Inertial Confinement Fusion (ICF) implosion.¹ Unlike classical, weakly coupled plasmas, WDM is characterized by strong plasma particle correlations and may involve quantum mechanical effects (e.g., electron Fermi degeneracy).

Another phenomenon that many HED systems have in common is the appearance of shocks; which is particularly the case for ICF. While the structure of a plasma shock in weakly coupled plasmas (with purely classical electrons and ions) has been well explored,^{2–10} to our knowledge, no results for any WDM regime have been published. We aim to rectify this by reporting the first results for a hydrodynamic simulation of a strong, steady-state, planar plasma shock in a WDM regime characterized by strongly coupled ions and fully Fermi degenerate electrons.

We acknowledge that strong shocks are intrinsically kinetic in nature and that the hydrodynamic (i.e., continuum) approach will not capture these effects. However, as a first step toward uncovering the structure of WDM shocks, we follow the historical precedent^{2–5} established by the study of non-degenerate/weakly coupled shocks, by first considering the hydrodynamic approach. Limitations of hydrodynamic modeling aside, we show that the WDM shock structure displays some notable differences from the non-degenerate/weakly coupled continuum solution.

Another advantage to using the hydrodynamic limit is the fact that, via the Green–Kubo^{11,12} relations, equilibrium molecular dynamics (MD) simulations can be used to calculate the ion transport coefficients in the strong Coulomb coupling regime. Equilibrium MD can also be used to infer the ion equation of state (EOS).

The paper is organized as follows. Section II reviews the basic structure of plasma shocks in the weakly coupled, purely classical limit. Section III describes the basic physics parameters and orderings which confine the WDM subspace we consider in this study. Next, Sec. IV details the fluid equations we use to simulate a WDM shock. Then, Sec. V considers subtleties surrounding the meaning of the mean-free-path in a strongly coupled regime and presents a resolution. Section VI explains the hydro code, *SHion*, which we use for our simulations. After that, Sec. VII shows our main results, which make it clear that the structure of a WDM shock differs from the non-degenerate/weakly coupled equivalent. We address the uncertainties in our EOS model in Sec. VIII and consider the impact of kinetic effects on the plasma structure in Sec. IX. Finally, we conclude in Sec. X. All equations appear in cgs units.

II. REVIEW OF COLLISIONAL PLASMA SHOCKS

We start with a review of collisional plasma shocks. To our knowledge, the structure of plasma shocks has only been studied in the non-degenerate/weakly coupled plasma regime. Multiple authors^{2–5} have shown that the hydrodynamic structure of a strong (non-radiative and non-magnetized), planar, steady-state plasma

shock can be divided into three distinct regions. These are (1) an electron preheat layer, in which the electron temperature exceeds the ion temperature in the front part of the shock, of length $\sim \sqrt{m_i/m_e} \lambda_{ii}$ —where m_i and m_e are the ion and electron mass, respectively, and λ_{ii} is the post-shock (downstream) ion–ion mean free path (mfp); (2) an ion compression shock of a few λ_{ii} in length, wherein the plasma density is compressed by a factor of about 4 (for shocks in monatomic ideal gases; like weakly coupled plasmas), and the electrons are heated quasi-adiabatically; (3) a layer behind the shock where the ion and electron temperatures equilibrate—which is also of length $\sim \sqrt{m_i/m_e} \lambda_{ii}$ (see Fig. 1).

As we expand upon in Sec. IX, plasma kinetic effects cause the structure of a shock to differ from the hydrodynamic picture,^{6–8,10} by smearing out the sharp features near sites of strong gradients (see Fig. 2).

Nonetheless—as Fig. 2 attests—the basic division into three distinct regions remains. For our study—which approaches shock structure from the hydrodynamic perspective—it will be the non-degenerate/weakly coupled fluid results which provide our reference point.

III. BASIC PHYSICS CONSIDERATIONS

For our main results, we will consider hydrogen plasma, only. However, for the sake of generality, let us first consider a generic single-ion plasma (labels “i” and “e” signify the ion and electron species s , respectively) in a non-magnetized, non-radiative, non-relativistic plasma with strongly coupled, classical ions and fully Fermi degenerate electrons. This represents a subspace of the WDM regime. The ion coupling strength is then fully determined by the Coulomb coupling parameter

$$\Gamma_i \equiv \frac{Z_i^2 e^2}{a T_i}, \tag{1}$$

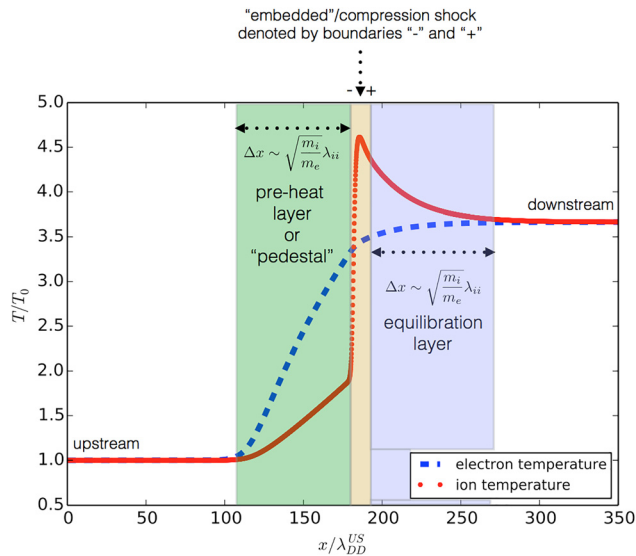


FIG. 1. Normalized temperature profiles for a non-degenerate/weakly coupled, single-ion, hydrogen plasma shock with $M \gg 1$ at steady state in a planar geometry. T_0 is the upstream temperature, and λ_{DD}^{US} is the upstream ion–ion mean-free-path. Reproduced with permission from Keenan *et al.*, Phys. Rev. E **96**, 053203 (2017). Copyright 2017 American Physical Society.

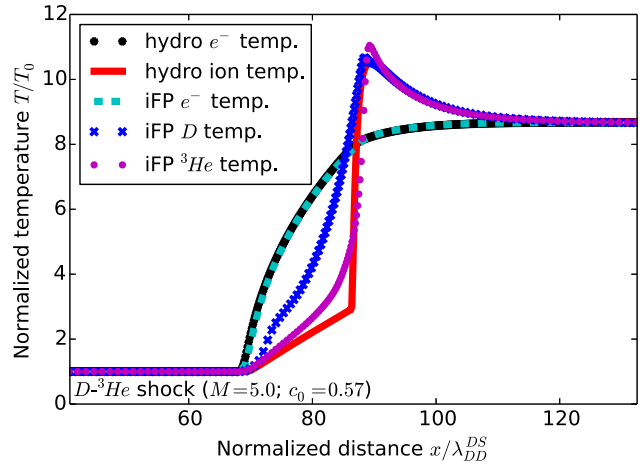


FIG. 2. Normalized temperature profiles for a non-degenerate/weakly coupled, $D\text{-}^3\text{He}$, hydrogen plasma shock with $M=5$ at steady state in a planar geometry. Here, the solutions labeled *iFP* are from a Vlasov–Fokker–Planck code—which is fully kinetic for the ions, but uses a fluid electron model. The hydro curves are obtained from the *SHion* shock code. Reproduced with permission from Keenan *et al.*, Phys. Rev. E **96**, 053203 (2017). Copyright 2017 American Physical Society.

where T_i is the ion temperature, $e \equiv |e|$ is the elementary electric charge, and $Z_i \equiv q_i/e$ —where q_i is the net ion charge, and

$$a = [3/(4\pi n_i)]^{1/3}, \tag{2}$$

is the Wigner–Seitz radius (i.e., the average separation distance between plasma particles)—where n_i is the ion number density. Ions occupy the moderate to strong coupling regime when $\Gamma_i \gtrsim 1$.

Next, the impact of electron degeneracy depends upon two key parameters: (1) the Fermi temperature¹³

$$T_F \equiv \frac{2}{3} \epsilon_F = \left(\frac{\pi^{4/3} \hbar^2}{3^{1/3} m_e} \right) n_e^{2/3}, \tag{3}$$

where $\hbar = h/(2\pi)$ is the reduced Planck’s constant, m_e is the electron mass, n_e is the electron number density, and ϵ_F is the Fermi energy and (2) the Thomas–Fermi screening length¹³

$$\lambda_{TF} = \left(\frac{\pi}{3n_e} \right)^{1/6} \frac{\hbar}{2Z_i e m_e^{1/2}}. \tag{4}$$

If the electron temperature $T_e \ll T_F$, and $a \ll \lambda_{TF}$, then, the electrons are strongly Fermi degenerate. In this case, the degenerate electrons largely serve as a neutralizing background for the ions. This is the regime where the one-component plasma (OCP) accurately describes the ion state.¹³

In the opposite limit of $a \gg \lambda_{TF}$ and $T_e \gg T_F$, the ion and electron interactions are mostly classical unless an electron–ion pair approach each other within their de Bröglie wavelengths, λ_e and λ_i , at which point, effects like quantum diffraction become important. These effects, however, can be approximated via the use of an effective potential for a two-component (i.e., ion + electron) plasma (TCP).¹³

Finally, we can quantify the role of electron strong coupling effects using the Brueckner parameter, r_s —which is the ratio of the Wigner–Seitz radius to the Bohr radius¹⁴

$$r_s = a/a_B. \tag{5}$$

For a hydrogen plasma,

$$r_s = \frac{\Gamma_i}{2\pi} \left(\frac{a}{\lambda_e} \right)^2. \tag{6}$$

Electrons are weakly coupled when $r_s \ll 1$. To avoid complications associated with TCP in this study, we assume the following orderings

$$\Gamma_i \gtrsim 1, \tag{7a}$$

$$\frac{T_e}{T_F} \equiv \theta \lesssim 1, \tag{7b}$$

$$\lambda_{TF} \gtrsim a, \tag{7c}$$

$$r_s \lesssim 1, \tag{7d}$$

so that the local plasma equilibrium is well described by molecular dynamics (MD) simulations of just ions in a neutralizing background (provided by degenerate electrons). This then allows us to use OCP-type MD simulations to inform the models we adopt for ion transport coefficients and the ion EOS. Given the assumption of full electron degeneracy, we also employ the ideal Fermi gas EOS for the electrons and the Boltzmann–Ziman model^{15,16} (with a generalized Coulomb logarithm) for their thermal conductivity.

With National Ignition Facility (NIF) ICF implosions shots in mind, we plot the density and temperature range of a radiation-hydrodynamic simulation of NIF shot N170601¹⁷ in Fig. 3. The WDM subspace described by Eq. (7) roughly fits around the characteristic evolution curve of the D-T ice layer—as extracted from Rinderknecht *et al.*¹⁷ using Datathief III.¹⁸

Our ion MD simulations use the Yukawa-OCP model. This entails a simulation of just ions, all interacting via an effective (screened) potential. We use the following ion–ion potential¹⁹

$$U_{\alpha\beta} = \frac{Z_i^2 e^2}{r} \exp(-r/\lambda), \tag{8}$$

where α and β denote individual ion particles, and

$$\lambda^{-2} \equiv \frac{4\pi e^2 n_e}{\sqrt{T_e^2 + T_F^2}}, \tag{9}$$

is an effective screening length which bridges the gap from the classical (i.e., Debye-type) to the fully degenerate (i.e., Thomas–Fermi-type) screening regimes.

Despite the fact that we treat the electrons as a neutralizing background in our MD simulations, we still allow $T_i \neq T_e$ (where T_i is the ion temperature) in our fluid shock simulation. We believe that this assumption is justified in the regime of interest since the ion EOS and transport coefficients are largely independent of the electron dynamics. This is certainly the case in weakly coupled plasmas, where ion–ion collisions exclusively determine the ion transport coefficients (i.e., viscosity). Admittedly, however, correlation effects between ion and electrons can be very consequential in strongly coupled plasmas. In other words, ion–electron interactions can make a Virial contribution to the ion transport coefficients and EOS.

Nevertheless, by using an effective MD potential (as we do here), the impact of ion–electron correlations on ion transport and the EOS can be emulated—as long as these correlations remain relatively weak. In this respect, $T_e \neq T_i$ is handled via Eq. (8) by using a separate electron temperature to define the screening length, and it is thereby assumed that any weak ion–electron correlations impact transport and EOS properties exclusively via the effective ion–ion potential.

Nevertheless, while only weak ion–electron correlations may be present within the shock front itself, ion–electron temperature equilibration occurs downstream of the plasma shock. Fortunately, we can approximate the impact of ion–electron correlations on thermal equilibration by using a generalized, i.e., Coulomb logarithm (informed by dedicated TCP MD simulations²⁰).

As a final consideration, we note that the plasma ionization state can vary across a WDM shock. For this study, we will ignore this effect and assume that Z_i remains constant throughout the entirety of the WDM shock.

Having elucidated the microphysics underlying our EOS and transport models, we describe the fluid equations used to simulate a hydrogen ($Z_i = 1$) WDM shock in Sec. IV.

IV. PLASMA FLUID EQUATIONS

To simulate a plasma shock in the WDM regime, we appeal to the equations of hydrodynamics. Since we allow $T_i \neq T_e$, we will require a set of equations for both the ions and the electrons. First, we describe the ion fluid equations in the following.

A. Ion hydrodynamic treatment

Allowing $T_i \neq T_e$ means that we require separate evolution equations for the protons and electrons. The ion quantities (mass density, temperature, and flow velocity) can be obtained from the total plasma continuity equations. By imposing quasi-neutrality, and ignoring electron inertia, only the electron energy equation is then required to close the system.

With a focus on the ion physics, we note that the total plasma mass continuity, momentum, and energy equations are given by^{21–24}

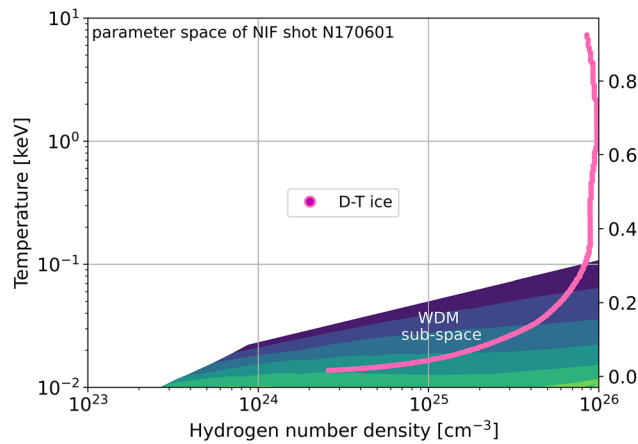


FIG. 3. A selection of the range of temperatures and densities visited by a radiation-hydrodynamic simulation of NIF shot N170601.¹⁷ The shaded area represents the sub-space which abides by the WDM orderings from Eq. (7), and the magenta curve is the characteristic path of the D–T ice layer through ρ – T space. The leftmost edge of this curve represents the time of the main shock rebound from the capsule center, and the rightmost edge is near peak thermonuclear reactivity.

$$\partial_t \rho + \nabla \cdot (\rho \mathbf{u}) = 0, \tag{10a}$$

$$\partial_t (\rho \mathbf{u}) + \nabla \cdot (\rho \mathbf{u} \otimes \mathbf{u}) + e(Z_i n_i - n_e) \mathbf{E} = -\nabla \cdot \bar{\sigma}, \tag{10b}$$

$$\partial_t (n_i \mathcal{E}_i + n_e \mathcal{E}_e) + \nabla \cdot (n_i \mathcal{E}_i \mathbf{u} + n_e \mathcal{E}_e \mathbf{u} + \mathbf{q} + \mathbf{u} \cdot \bar{\sigma} \leftrightarrow \sigma) = \mathbf{J} \cdot \mathbf{E}, \tag{10c}$$

where $\rho \equiv \rho_i + \rho_e = m_i n_i + m_e n_e \approx m_i n_i$ is the plasma mass density (n_s denotes a number density for species, $s = i, e$), \mathbf{u} is the bulk fluid velocity, Z_i is the assumed constant, \mathbf{E} is the macroscopic (Vlasov) electric field, \mathbf{J} is the electric current density, \mathcal{E} is the total plasma internal energy, and $\bar{\sigma}$ is the plasma stress tensor, defined by

$$\begin{aligned} \nabla \cdot \bar{\sigma} = & \nabla p - \nabla \cdot \left\{ \sum_s \eta_s [\nabla \mathbf{u} + (\nabla \mathbf{u})^T] \right\} \\ & + \nabla \cdot \left\{ \sum_s \left(\frac{2}{3} \eta_s - \mu_b^s \right) \nabla \cdot \mathbf{u} \right\} - \sum_s n_s \mathbf{F}_s^C(\mathbf{x}, t), \end{aligned} \tag{11}$$

wherein, the sum is over both ions and electrons, η_s is the species shear viscosity, μ_b^s is the species bulk viscosity, $p \equiv p_e + p_i$ is the total pressure (where p_e and p_i are the electron and ion pressures, respectively), and \mathbf{F}_s^C is the Coulomb force between a particle of species, s , and all other particles, which has the form²⁴

$$\mathbf{F}_s^C(\mathbf{x}, t) = -e^2 \sum_{s'} \int d\mathbf{x}' \nabla \left[\frac{Z_s Z_{s'}}{|\mathbf{x} - \mathbf{x}'|} \right] n_{s'}(\mathbf{x}', t); \tag{12}$$

where Z_s can be either Z_i or $Z_e = -1$, and

$$p_i \equiv n_i T_i - \frac{1}{6} n_i^2 \int d^3 r r h(r) \frac{dU}{dr}, \tag{13}$$

where U is given by Eq. (8).

The second term on the RHS of Eq. (13) is called the excess pressure^{13,24} and h is the ion–ion pair correlation function. Let us define

$$\alpha(n_i, T_i, T_e) \equiv -\frac{1}{6} \frac{n_i}{T_i} \int d^3 r r h(r) \frac{dU}{dr}, \tag{14}$$

so that we may write

$$p_i = (1 + \alpha) n_i T_i = p_i^k + \alpha p_i^k, \tag{15}$$

where $p_i^k \equiv n_i T_i$ is the ion kinetic pressure. Note that Eq. (14) applies strictly to a homogeneous medium. More specifically, accounting for weak spatial inhomogeneity, the total ion pressure becomes²⁴

$$p \approx n_i T_i - \frac{2\pi}{3} n_i^2 \int s^3 \frac{dU}{ds} h^0(s) ds - \frac{2\pi}{3} n_i \nabla n_i \int s^4 \frac{dU}{ds} h^0(s) ds, \tag{16}$$

where h^0 is the local pair correlation function. The local pair correlation function is not available to use directly in a hydrodynamic simulation—although it can be readily post-processed (e.g., via MD simulations, or a hypernetted chain solve) after the fact. For this reason, we will ignore this non-local correlation effect on the ion EOS. However, this assumption likely fails within the compression shock, but we leave further investigation of this to a future study.

Next, to first order (i.e., ignoring spatial gradients in the ion temperature/density, and electron inertia), the total internal energy density is

$$n_i \mathcal{E}_i + n_e \mathcal{E}_e = \frac{3}{2} p^k + \frac{1}{2} \rho u^2 + 3\alpha n_i T_i, \tag{17}$$

where $p^k \equiv p_i^k + p_e$ is the total kinetic pressure.

Finally, $\mathbf{q} \equiv \mathbf{q}_i + \mathbf{q}_e$ is the total heat flux, where

$$\mathbf{q}_s = -\kappa_s \nabla T_s, \tag{18}$$

in which κ_s is the species coefficient of the thermal conductivity.

To proceed, we need to further deconstruct the plasma stress tensor, Eq. (11). Fortunately, we can make a few simplifying assumptions. First, we note that while the ion bulk viscosity is zero for weakly coupled plasmas, in principle, it may assume non-zero values for $\Gamma_i \gtrsim 1$. However, it has been shown that $\mu_b^i \ll \eta_i$ in the OCP for $\Gamma_i \in (1, 160)$,²⁶ and μ_b^i is nearly zero by magnitude.²⁷ Consequently, abiding by the Stokes' hypothesis, we may take $\frac{2}{3} \eta_i - \mu_b^i \approx \frac{2}{3} \eta_i$ in Eq. (11)—i.e., we ignore the ion bulk viscosity, μ_b^i .

Furthermore, we assume that $\eta_i \gg \eta_e$ and that μ_b^e can be neglected. The first assumption is definitely true for very low- Z plasmas, but μ_b^e could—in principle—be large for degenerate electrons. Preliminary comparisons with established theory¹⁶ indicate that $\mu_b^e \ll \eta_i$ in the WDM regime of interest, but we leave the details to a future study.

Next, if we assume quasi-neutrality, $n_e = Z_i n_i$; thus, the electric field term disappears from the total plasma momentum equation.

Similarly, the $\mathbf{F}_s^C(\mathbf{x}, t)$ term vanishes as well since

$$\mathbf{F}_i^C(\mathbf{x}, t) = -Z_i e^2 \int d\mathbf{x}' \nabla \left[\frac{1}{|\mathbf{x} - \mathbf{x}'|} \right] (Z n_i - n_e) = 0, \tag{19}$$

and the same results for $\mathbf{F}_e^C(\mathbf{x}, t)$.

Another consequence of charge conservation and quasi-neutrality is ambipolarity: $\nabla \cdot \mathbf{J} = 0$. If we additionally consider a 1D geometry for the shock, $\mathbf{J} = 0$, and so $\mathbf{J} \cdot \mathbf{E} = 0$ (this also implies that: $\mathbf{u} = \mathbf{u}_i = \mathbf{u}_e$). Consequently, we do not need an additional equation for the electric field since it vanishes from Eqs. (10).

Finally, we must make a choice for the ion shear viscosity and thermal conductivity coefficients. For this, we elect to use the Stanton–Murrillo²⁸ transport model. This model is informed by Yukawa-OCP MD simulations and the Boltzmann transport theory.

B. Electron hydrotreatment

For weakly coupled electrons, it can be shown that²¹

$$\partial_t \left(\frac{3}{2} p_e \right) + \nabla \cdot \left(\frac{3}{2} p_e \mathbf{u} - \kappa_e \nabla T_e \right) + p_e \nabla \cdot \mathbf{u} = g(T_i - T_e), \tag{20}$$

where κ_e is the electron thermal conductivity and g is the electron–ion relaxation rate.

Equation (20) is obtained from substituting the ambipolar electric field—obtained from the electron momentum equation in the $m_e \rightarrow 0$ limit—into the electron energy equation. Additionally, the electron mass continuity equation may be ignored as $m_e n_e \approx 0$. Thus, only the modified electron energy equation—Eq. (20)—is needed to close the plasma fluid equations.

Note that we omit the electron viscosities, η_e and μ_b^e , from Eq. (20). The electron shear viscosity contribution for non-degenerate/weakly coupled hydrogenic plasma shocks is negligible compared to the other terms,¹⁰ so we assume that the same holds here. We assume that the μ_b^e contribution can, likewise, be neglected.

Since the electrons are assumed to be fully degenerate, they are described by the ideal Fermi EOS. Thus, the electron temperature is given by²⁹

$$T_e = \left(\frac{2\pi\hbar^2}{m_e} \right)^{3/5} \left[\frac{p_e}{f_{5/2}(z)} \right]^{2/5}, \quad (21)$$

where z (the fugacity) is unknown and $f_{5/2}(z)$ is the Fermi–Dirac integral²⁹

$$f_{5/2}(z) = \frac{4}{\sqrt{\pi}} \int_0^\infty dx x^2 \log(1 + ze^{-x^2}). \quad (22)$$

We appeal to quasi-neutrality, $n_e = Zn_i$, and the Fermi–Dirac equation for the density

$$n_e = T_e^{3/2} \left(\frac{m_e}{2\pi\hbar^2} \right)^{3/2} f_{3/2}(z), \quad (23)$$

where

$$f_{3/2}(z) = z \frac{\partial}{\partial z} f_{5/2}(z), \quad (24)$$

to find z by solving the equation

$$Zn_i = \left(\frac{m_e}{2\pi\hbar^2} \right)^{3/5} \left[\frac{p_e}{f_{5/2}(z)} \right]^{3/5} f_{3/2}(z). \quad (25)$$

Next, we need an expression for the electron thermal conductivity κ_e . We use the Boltzmann–Ziman hydrogen conductivity^{15,16}

$$\kappa_e = A_\kappa \left(\frac{n_e T_e}{m_e} \right) \left(\frac{3\pi\hbar^3}{4m_e e^4} \right) 2G(q_F), \quad (26)$$

where $A_\kappa \equiv \pi^2/3$, $G(q_F)$ is a function which depends upon the OCP structure factor (which is related to the Fourier image of the ion–ion pair correlation function), and $q_F = k_F a$ —with k_F being the Fermi wave-number at zero temperature (cf. the fully degenerate transport coefficients in the high- Z Lee–More model³⁰).

The Boltzmann–Ziman model is valid in the fully degenerate limit for hydrogen, where electron–electron collisions can be ignored via the Pauli exclusion principle, and the Wiedemann–Franz relation between the electron thermal and electric conductivities holds. The Wiedemann–Franz relation is satisfied in a hydrogen plasma for $\theta \geq 0.1$.³¹

The structure factor term, $2G(q_F)$, may be treated as the multiplicative inverse of a generalized Coulomb log, $\ln(\Lambda_{ei})^*$. We elect to use^{20,32}

$$\ln(\Lambda_{ei})^* = \log(1 + b_{\max}/b_{\min}), \quad (27)$$

where

$$b_{\min} = \max \left(1.31 \frac{Ze^2}{T_{\text{BCH}}}, 0.78 \frac{\hbar}{\sqrt{m_e T_{\text{BCH}}}} \right) \quad (28)$$

and

$$b_{\max} = \sqrt{\frac{T_{\text{BCH}}}{4\pi n_e e^2}} \quad (29)$$

with $T_{\text{BCH}} \equiv \sqrt{T_e^2 + T_F^2}$. With these choices, we may re-write Eq. (26) as

$$\kappa_e = A_\kappa \left(\frac{n_e T_e \tau_F}{m_e} \right), \quad (30)$$

where

$$\tau_F = \frac{3\pi\hbar^3}{4m_e e^4 \ln(\Lambda_{ei})^*}, \quad (31)$$

is an effective electron–ion thermal relaxation time, which is equal to the Lee–More³⁰ ν_{ei}^{-1} in the fully degenerate limit (which we assume here).

Finally, we need an equation for g . By analogy to the classical limit, we take

$$g \approx 3 \left(\frac{m_e}{m_i} \right) n_e \tau_F^{-1}, \quad (32)$$

which is the standard Braginskii form.²¹ but with an electron–ion collision frequency given by τ_F^{-1} . Note, for simplicity, we use the same generalized electron–ion Coulomb log, Eq. (27).

C. Simplified electrons

The orderings in Eq. (7) can be used to simplify the Fermi pressure, Eq. (21). For $\lambda_e \gg a$, it can be shown that²⁹

$$p_e \approx \frac{2}{5} n_e \epsilon_F \left[1 + \frac{5\pi^2}{12} \left(\frac{T_e}{\epsilon_F} \right)^2 \right]. \quad (33)$$

For $\lambda_e \gtrsim a$, Eq. (33) is not necessarily accurate. For our shock simulation, we use the Zimmerman³³ fit to the ideal Fermi chemical potential

$$\frac{\mu_{\text{pot}}}{T_e} = \ln y_a + 0.3536y_a - 0.00495y_a^2 + 0.000125y_a^3, \quad y_a < 5.5; \quad (34a)$$

$$\frac{\mu_{\text{pot}}}{T_e} = 1.209y_a^{2/3} - 0.6803y_a^{-2/3} - 0.85y_a^{-2}, \quad y_a \geq 5.5, \quad (34b)$$

where $y_a = n_e (h/\sqrt{2\pi m_e T_e})^3 / 2$ and $e^{\mu_{\text{pot}}} = z$.

Then, with z calculated, we use the excellent fit to the Fermi integrals given by Aymerich-Humet *et al.*³⁴

D. 1D ion equations

Considering for now a 1D planar geometry, Eq. (10) simplifies to

$$\frac{\partial \rho}{\partial t} + \frac{\partial(\rho u)}{\partial x} = 0, \quad (35a)$$

$$\frac{\partial(\rho u)}{\partial t} + \frac{\partial}{\partial x} \left[\rho u^2 + p^k - \frac{4}{3} \eta \frac{\partial u}{\partial x} \right] = - \frac{\partial}{\partial x} (a n_i T_i), \quad (35b)$$

$$\begin{aligned} \frac{\partial}{\partial t} \left[\frac{3}{2} p^k + \frac{1}{2} \rho u^2 \right] + \frac{\partial}{\partial x} \left[\frac{5}{2} p^k u + \frac{1}{2} \rho u^3 + q - \frac{4}{3} \eta u \frac{\partial u}{\partial x} \right] \\ = -4 \frac{\partial}{\partial x} (a n_i T_i u) - 3 \frac{\partial}{\partial t} (a n_i T_i), \end{aligned} \quad (35c)$$

with $q = -\kappa_e \partial_x T_e - \kappa_i \partial_x T_i$, $p^k = n_i T_i + p_e$, and where we have isolated the excess pressure terms—unique to strong/moderate coupling—on the RHS in the momentum and energy equations.

E. Reference frame and boundary conditions

We consider planar shocks moving through a homogeneous medium and perform our calculations in the rest frame of the shock (i.e., the frame that moves at the constant shock speed, u_0). Thus, in the steady-state $\partial_t = 0$, everything else (in all three ion equations) is a total derivative (∂_x) equal to zero. Thus, the momentum equation—for example—becomes

$$\rho u^2 + p^k - \frac{4}{3}\eta \frac{\partial u}{\partial x} + \alpha n_i T_i = \rho_0 u_0^2 + p_e^0 + (\alpha_0 + 1)n_0 T_0, \quad (36)$$

where 0 denotes the upstream (pre-shock) values. This is a generalization of the famous Rankine–Hugoniot (jump) condition for momentum conservation.

Sufficiently downstream of the shock (i.e., the post-shock region), the hydro gradients will vanish (and the ion and electron temperatures will be equilibrated), meaning that

$$\rho_1 u_1^2 + (1 + \alpha_1)n_1 T_1 + p_e^1 = \rho_0 u_0^2 + (1 + \alpha_0)n_0 T_0 + p_e^0, \quad (37)$$

where 1 denotes the downstream values. Because $T_e^1 = T_i^1 = T_1$, we do not need the electron energy equation, Eq. (20), to specify the boundary conditions in the shock frame.

Similarly, the pre/post-shock jump condition for mass conservation is

$$\rho_1 u_1 = \rho_0 u_0, \quad (38)$$

and for energy

$$\begin{aligned} \frac{5}{2}n_1 T_1 u_1 + 4\alpha_1 n_1 T_1 u_1 + \frac{5}{2}p_e^1 u_1 + \frac{1}{2}\rho_1 u_1^3 \\ = \frac{5}{2}n_0 T_0 u_0 + 4\alpha_0 n_0 T_0 u_0 + \frac{5}{2}p_e^0 u_0 + \frac{1}{2}\rho_0 u_0^3. \end{aligned} \quad (39)$$

The set of Eqs. (37)–(39) define the boundary conditions used in our steady-state, planar shock simulations described in Sec. VII.

F. Ion EOS

Finally, to close the system of Eqs. (35c) and (20), we need an expression for the excess ion pressure $p_{ex}^i \equiv \alpha(n_i, T_i, T_e)n_i T_i$. For what follows, we consider only single-ion hydrogen plasmas (hence, the ions are protons).

To that end, we have performed a number of Yukawa–OCP MD simulations using LAMMPS.³⁵ We present the results over a range of Γ_i and $\theta = T_e/T_F$ in Fig. 4.

Figure 4 also shows a fit to the LAMMPS data to a DWSC-type (DeWitt, Slattery, and Chabrier)³⁶ OCP model—which is a function of Γ_i , only. The DWSC model is given by

$$\alpha_{\text{DWSC}} = a\Gamma_i + b\Gamma_i^s + c, \quad (40)$$

where $a = -0.899126$, $b = 0.60712$, $c = -0.27998$, and $s = 0.321308$. The DWSC model is an accurate fit of the OCP α , with $1 \leq \Gamma_i \leq 160$.

Despite the accuracy of α_{DWSC} , however, it is not a good fit to our Yukawa–OCP-derived data. The reason for this is that the use of an effective potential emulates the proton–electron contributions to the proton pair correlation functions, and as a consequence, our system differs from the bare Coulomb OCP model which informs the DWSC fit.

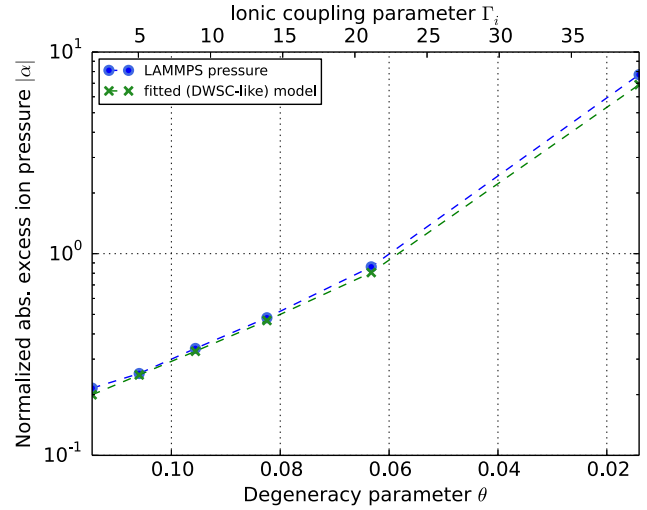


FIG. 4. The normalized excess proton pressure, α vs the ionic coupling parameter, Γ_i and the electron degeneracy parameter, θ . The blue circles are obtained from LAMMPS Yukawa–OCP MD simulations, and the green crosses are from the fit function: $\alpha_{\text{fit}} = -0.17651319\Gamma_i + 0.11731267$.

Nonetheless, we find that new values of a , b , c , and s are a great fit to the LAMMPS data. These values are $a = 46.27446501$, $b = -46.4509782$, $c = 0.11731267$, and $s = 1.00012267$. To simplify the inversion of the proton EOS (i.e., to calculate the proton temperature, T_i), we take $s = 1$. As s is very close to one, this has a mostly negligible effect on the fit (which is shown in Fig. 4 as the green crosses) for $\Gamma_i \leq 10$.

In Sec. VI, we describe the single-purpose hydrodynamic code we developed to perform our shock simulation, *SHion*.

V. CONCERNING THE MEAN-FREE-PATH IN STRONGLY COUPLED SYSTEMS

The mean-free-path (mfp) in weakly coupled systems is the mean distance a plasma particle of species, s , travels—with a typical speed given by its thermal velocity, $v_{th,s} = \sqrt{2T_s/m_s}$ —before its initial velocity vector is deflected by an angle of 90° . Since particle collisions are largely just grazing in weakly coupled plasmas, in order for Coulomb collisions to radically alter a plasma particle’s trajectory, many collisions need to happen in succession (hence, the criterion of a 90° deflection). Individual collisions occur on a timescale comparable to the species’ plasma frequency, $\omega_{ps} = \sqrt{4\pi n_s/m_s}$, but a “collision time,” τ_{90° is considerably longer.

In contrast, strongly coupled plasmas have strong Coulomb collisions. These collisions are not necessarily grazing so that τ_{90° is no longer a meaningful metric. Nonetheless, a thorough examination of WDM shocks will require some definition for the strongly coupled ion mfp.

To this end, we appeal to the experimental results of Bannasch *et al.*,³⁷ who measured the velocity relaxation time for a strongly coupled ion plasma with degenerate electrons. By normalizing the relaxation time to the inverse plasma frequency, Bannasch *et al.*³⁷ developed an accurate fit to their observations across multiple ion couplings, which they plotted in Fig. 5. Using Datathief III,¹⁸ we extracted relaxation times from the Bannasch *et al.*,³⁷ fit.

Given the extracted relaxation times, τ_B as the effective collision time, we define the Bannasch mfp as

$$\lambda_B = v_{th} \tau_B. \quad (41)$$

As we show in Sec. VII, Eq. (41) does have a natural correspondence to the non-degenerate, weakly coupled equivalent.

VI. DESCRIPTION OF THE SHION HYDRO CODE

To simulate a planar WDM shock in its steady state, we use a dedicated hydro solver, which we call *SHion*. This code is a modification of the shock hydro code described in Simakov *et al.*²¹ and Keenan *et al.*^{8,38}

This single-purpose hydro code—which uses backward Euler implicit time-stepping and an upwinding scheme for the spatial derivatives—was created to simulate planar, steady-state, multi-ion plasma shocks with non-degenerate, weakly coupled ions and electrons. Thus, the code normalizations are framed from that perspective. For convenience, we retain these basic normalizations, but with WDM modifications, as needed.

As in the original code, the spatial coordinate, x , is normalized to the (non-degenerate, weakly coupled) mfp in the upstream region, λ_0^{wc} ; in other words,

$$\hat{x} \equiv S_f \frac{x}{\lambda_0^{wc}}, \quad (42)$$

where S_f is a computational scale factor. Here, and elsewhere, we denote quantities defined with respect to non-degenerate/weakly coupled systems by the sub/superscript, wc .

Next, although λ_0^{wc} is arbitrary, considerable simplification of the hydrodynamic equations is achieved by choosing it to be the proton–proton mfp in the upstream region, $\lambda_0^{wc} = v_{thH}^0 / \nu_{HH0}^{wc}$ —where v_{thH}^0 and ν_{HH0}^{wc} are the upstream proton thermal velocity and proton–proton collision frequency, respectively. For simplicity, we use a constant reference Coulomb log of 10 in ν_{HH0}^{wc} . Note that, as discussed in Sec. V, ν_{HH0}^{wc} does not have any clear meaning in the strongly coupled regime. Nonetheless, for ease of translating the normalized equations to strong-coupling, we retain this normalization.

This choice for \hat{x} , similarly, allows us to write the time normalization as

$$\hat{t} \equiv S_f \frac{u_0 t}{\lambda_0^{wc}}, \quad (43)$$

where, as before, u_0 is the shock velocity in the lab frame.

Additionally, we normalize all pressures to $p_0^{wc} = (Z_i + 1)n_0 T_0$, which is the total ideal plasma pressure upstream. Then, the (ideal) upstream sound speed is

$$c_{s0}^{wc} = \sqrt{\gamma p_0^{wc} / \rho_0}, \quad (44)$$

where $\gamma = 5/3$ is the classical, ideal adiabatic index. So,

$$M_{wc} \equiv \frac{u_0}{c_{s0}^{wc}} \quad (45)$$

is the plasma Mach number, as defined under the assumption that the plasma is non-degenerate and weakly coupled. Note that the true shock Mach number within a WDM plasma will differ from M_{wc} for any given u_0 since the sound speed is different.

Given these normalizations, the electron energy equation becomes

$$\frac{3}{2} \partial_i \hat{p}_e + \partial_x \left[\frac{3}{2} \hat{p}_e \hat{u} - \hat{\kappa}_e \partial_x \hat{T}_e \right] + \hat{p}_e \partial_x \hat{u} = \hat{g} (\hat{T}_i - \hat{T}_e), \quad (46)$$

where $\hat{u} \equiv u/u_0$, $\hat{\rho} \equiv \rho/\rho_0$, $\hat{p}_e \equiv p_e/p_0^{wc} = p_e/[(Z_i + 1)n_0 T_0]$, $\hat{T}_e \equiv T_e/T_0$, and $\hat{T}_i \equiv T_i/T_0$. The normalized electron thermal conductivity, $\hat{\kappa}_e$, and the electron–ion thermal equilibration rate, \hat{g} , are given by normalized versions of Eqs. (26) and (32), respectively.

The normalized electron transport coefficients are given in Simakov *et al.*²¹ but with a few modifications. Aside from constant numerical factors, the coefficients differ only in the definition of the electron–ion collisional timescale. Letting $\hat{\tau}_F$ represent the Fermi collision time, and $\hat{\tau}_{ei} \equiv \hat{\nu}_{ei}^{-1}$ the original Simakov e–i collision time, the two scales are related by

$$\frac{\tau^F}{\tau^S} = \sqrt{\frac{6}{\pi}} \hat{\theta}^{-3/2} \left(\frac{\hat{\rho}}{\hat{T}_e^{3/2}} \right), \quad (47)$$

where $\hat{\theta} \equiv \theta/\theta_0$.

Next, the total plasma equations (which we use to solve for the ion quantities) become

$$\partial_i \hat{\rho} = -\partial_x (\hat{\rho} \hat{u}), \quad (48a)$$

$$\partial_x [\hat{p} + \gamma M_{wc}^2 \hat{\rho} \hat{u}^2 - \hat{\eta}_i \partial_x \hat{u}] = -\partial_i (\hat{\rho} \hat{u}), \quad (48b)$$

$$\begin{aligned} \partial_x \left[\left(\frac{5}{2} \hat{p}^k + 4 \hat{p}_{ex}^i \right) \hat{u} + \frac{1}{2} \gamma M_{wc}^2 \hat{\rho} \hat{u}^3 + \hat{q}_i + \hat{q}_e - \hat{\eta}_i \hat{u} \partial_x \hat{u} \right] \\ = -\partial_i \left[\frac{3}{2} \hat{p}^k + 3 \hat{p}_{ex}^i + \frac{1}{2} \gamma M_{wc}^2 \hat{\rho} \hat{u}^2 \right], \end{aligned} \quad (48c)$$

where $\hat{p}_{ex}^i \equiv \hat{p}_i - \hat{p}_k = \alpha \hat{\rho} \hat{T}_i / (Z_i + 1)$ and $\hat{\eta}_i$ is defined in Simakov *et al.*²¹—with the caveat that we use a generalized Coulomb log from the Stanton–Murillo²⁸ model here (Simakov *et al.*²¹ assume the same Coulomb log for all quantities). Similarly, $\hat{\kappa}_i$ is also given by Simakov *et al.*²¹ but also using a Stanton–Murillo²⁸ generalized Coulomb log.

At steady state—assuming constant Coulomb logs for all interactions—the structure of a shock within a non-degenerate/weakly coupled plasma will only depend upon M_{wc} . However, in the WDM regime, we must also add θ_0 and Γ_{i0} to describe a steady-state shock. Consequently, the space of possibilities is now $(M_{wc}, \Gamma_{i0}, \theta_0)$, which is significantly more vast. Fortunately, our assumed orderings, i.e., Eq. (7), do considerably narrow this space.

Finally, we can translate a normalized *SHion* solution (which depends upon M_{wc} , θ_0 , and Γ_i) using the following unit conversions

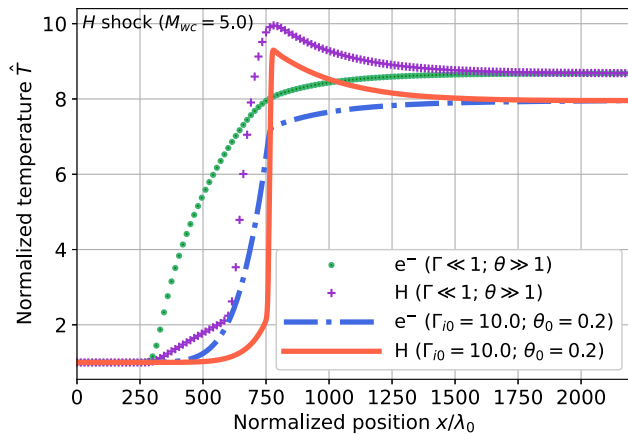
$$T_0 = (4\pi/3)^{1/3} \frac{e^2}{\Gamma_{i0}} n_0^{1/3} = 2.32 \times 10^{-7} \frac{n_0^{1/3} [\text{cm}^{-3}]}{\Gamma_{i0}} [\text{eV}], \quad (49a)$$

$$n_0 = 4\alpha_{fs}^3 \left(\frac{\theta_0^{-1}}{\pi \Gamma_{i0}} \right)^3 \left(\frac{m_e c}{\hbar} \right)^3 = 8.71 \times 10^{23} \left(\frac{\theta_0^{-1}}{\Gamma_{i0}} \right)^3 [\text{cm}]^{-3}, \quad (49b)$$

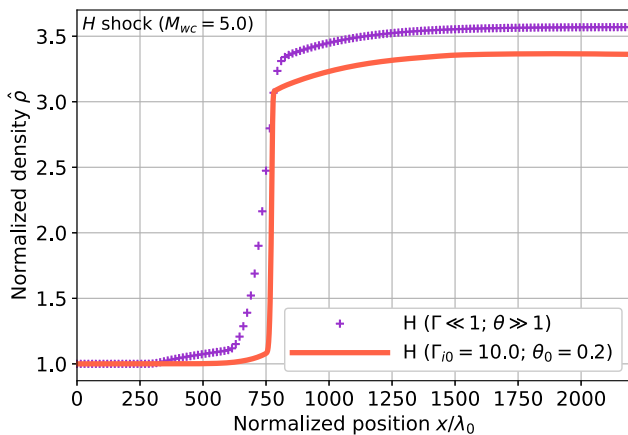
where α_{fs} is the fine structure constant.

VII. MAIN RESULTS

A major issue with simulating shock structure is the separation in scales across its distinct regions. Whereas the ion compression shock is the order of a few downstream mfps, the electron pre-heat layer and



(a) Proton and electron temperatures.



(b) Mass densities.

FIG. 5. Density and temperature profiles for a planar WDM shock with $\Gamma_{i0} = 10$, $\theta_0 \approx 0.2$, and $M_{wc} = 5$, and a non-degenerate/weakly coupled (all $\Gamma \ll 1$ and $\theta \gg 1$) Mach 5 planar shock—both at steady-state conditions. The abscissas for both plots is normalized to the upstream mean-free-path, as defined by Eq. (50).

thermalization layers are $\sim \sqrt{m_i/m_e}$ times larger in a shock with non-degenerate, weakly coupled ions and electrons. This separation is exacerbated by degenerate electrons; as they are—in some sense—more resistant to changes in temperature than their classical counterparts. This is evident from Eq. (33), which shows that the Fermi pressure is independent of temperature as $\theta \rightarrow 0$. Similarly, the weak dependence of τ_F —i.e., Eq. (30)—on temperature/density also implies that electron–ion thermal equilibration can occur at a very low rate compared to competing processes (e.g., ion–ion collisional equilibration, which has a stronger dependence upon high temperature and density).

Hence, given these considerations, not only is a large computational grid required to simulate the full extent of a WDM shock, but fine resolution is also required to resolve the compression shock.

Weighing computational costs, we have found that some set of parameters work well over others. Here, we present specific results for a hydrogen shock with $M_{wc} = 5$, $\Gamma_{i0} = 10$, and $\theta_0 \approx 0.2$ —which translates to $n_0 = 1.88 \times 10^{23} \text{ cm}^{-3}$ and $T_0 = 1.33 \text{ eV}$, in physical units. Fortunately, we find that shocks in the neighborhood of $3 \lesssim \Gamma_i \lesssim 10$ and $\theta \sim 0.1$ are very qualitatively similar.

Given a mild amount of pre-heat, $n_0 = 1.88 \times 10^{23} \text{ cm}^{-3}$ and $T_0 = 1.33 \text{ eV}$ are similar to the initial state of the cryogenic D–T nuclear fuel in a triple shell Revolver ICF capsule prior to the breakout of the first shock.³⁹ The Mach number of this shock is ~ 6 .

The computational domain size of the WDM shock simulation is $L = (120/S_f)\lambda_0$, with a resolution of $d\hat{x} = 0.05$ and $S_f = 10^{-4}$.

The shock solution is achieved by equilibrating an arbitrary profile (satisfying the jump boundary conditions) until the self-consistent steady-state solution is reached.

Figures 5(a) and 5(b) show the temperature and density profiles, respectively. These plots also show the results from an *SHion* simulation of an $M_{wc} = 5$ shock in a non-degenerate/weakly coupled plasma (wherein all $\Gamma \ll 1$, $\theta \gg 1$, and the Coulomb logs are set equal for all interactions). The boundary conditions for this shock are given by the respective jump conditions—i.e., Eqs. (37)–(39), with $\alpha = 0$ and $p_e = n_e T_e = Z_i n_i T_e = n_i T_e$. The proton and electron transport coefficients are those of Braginskii.

The profiles from both simulations have been normalized to their respective upstream proton–proton mfps; i.e.,

$$\begin{cases} \lambda_0 \equiv v_{th0}^{HH} / \nu_{HH1}^{wc} & \text{if } \Gamma \ll 1 \text{ and } \theta \gg 1, \\ \lambda_0 \equiv \lambda_B & \text{if } \Gamma_{i0} > 1 \text{ and } \theta_0 < 1, \end{cases} \quad (50)$$

where λ_B is the Bannasch mfp, as given by Eq. (41).

Visually, there are some striking similarities between the non-degenerate/weakly coupled and the WDM shocks. Although the jump conditions differ between the solutions (owing to the differences in the proton and electron EOSs), their respective thermalization layers are about the same length (in the normalized coordinate, λ_0). Since the non-degenerate/weakly coupled thermalization layer scales as $\sim \sqrt{m_i m_e} \lambda_{HH1}^{wc}$ —where λ_{HH1}^{wc} is the downstream proton–proton mfp—we can conclude that the WDM shock thermalization layer shows the analogous scaling, $\sqrt{m_i/m_e} \lambda_B^1$. While this result is not entirely surprising, it was not a foregone conclusion, given that the electron–proton thermalization time scales can differ considerably between the two regimes.

There are some notable differences between the shock solutions, however. For example, the non-degenerate/weakly coupled proton temperature has a more pronounced “pedestal” feature in its electron pre-heat layer. This is more smoothed out in the WDM shock (the same can be said of the density feature there).

Similarly, the temperature separation between the protons and electrons is smaller in the pre-heat layer for the WDM shock. This is likely due to the suppressed WDM electron heat flux, which no longer retains its $\propto \sqrt{m_i/m_e}$ advantage over the proton conduction,⁸ since $\kappa_e \propto T_e$ in this regime—whereas κ_i remains $\propto T_i^{5/2}$. The same reasoning explains why the WDM electron pre-heat layer is—relative to the Bannasch mfp—considerably shorter than the non-degenerate/weakly coupled equivalent.

Next, we look at the WDM shock proton and electron pressures in Fig. 6. In this case, we present our results in physical units, showing

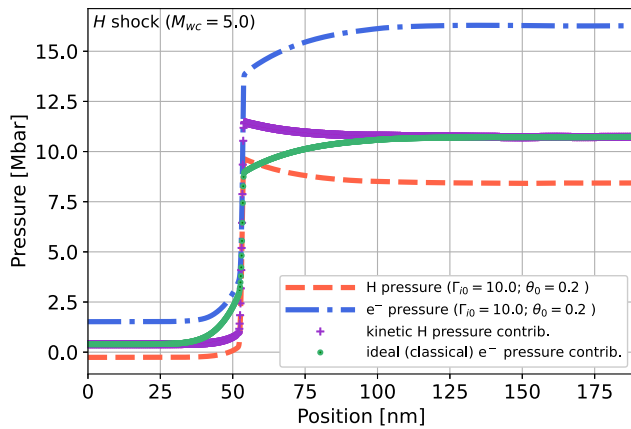


FIG. 6. The proton and electron pressures for a WDM shock with $\Gamma_{i0} = 10$, $\theta_0 \approx 0.2$, and $M_{wc} = 5$.

that the pressures in this WDM system are on the order of 1–10 Mbar. Additionally, we plot the ideal (kinetic) contributions to the pressures as well, showing that the excess proton pressure and the electron degeneracy contribute significantly.

Note that the physical scale of the WDM shock is ~ 100 nm in length. It should be noted that the proton shock width is then, accordingly, on the scale of a few nanometers. Only ~ 100 protons will fit into a region of ~ 1 nm at these densities. Hence, the continuum assumption likely breaks down within a few nanometers of the proton density jump (i.e., around 80 nm). Thus, the accuracy of the shock solution in this region, as well as the assumption of quasi-neutrality there, is in doubt. Nevertheless, as we show in Sec. IX, ion kinetic effects—which are, also, not accounted for by our hydrodynamic model—will probably smear out these sharp features near the compression shock in the real system. Hence, the overall effect is that the continuum limit is likely still satisfied in a WDM shock.

Troublingly, we note that $p_{ex}^i > n_i T_i$ in the upstream region—implying a negative total pressure there. While this may appear concerning at first, it is a common result for OCP plasmas. In fact, the DWSC model predicts a negative proton pressure at $\Gamma_i \approx 11.15$.

This negative pressure problem arises from ignoring the background’s contribution to the proton Virial.⁴⁰ As we show in Sec. VIII, properly accounting for the proton–electron contribution to the proton excess pressure restores positivity. Fortunately, we see no differences in the shock structure when the proton pressure is strictly positive.

Next, to test the accuracy of our proton EOS—relative to the Yukawa-OCP—we performed a number of LAMMPS simulations using the temperatures and densities extracted from our shock simulation. Figure 7 shows that our fitted α model does a decent job of matching LAMMPS. The strongest deviations are in the downstream region, but this is to be expected, as our fit is less accurate at small couplings, and $\Gamma_i \sim 2$ there (see Fig. 8 for a plot of Γ_i vs x). Notice that LAMMPS also predicts a negative pressure in the upstream region, albeit one that is closer to zero.

Finally, we address the adherence of our shock solution to our desired orderings—i.e., Eq. (7)—in Fig. 8. We note that $r_s \sim 2$ in the upstream, which indicates that non-ideal electron effects could be non-negligible.

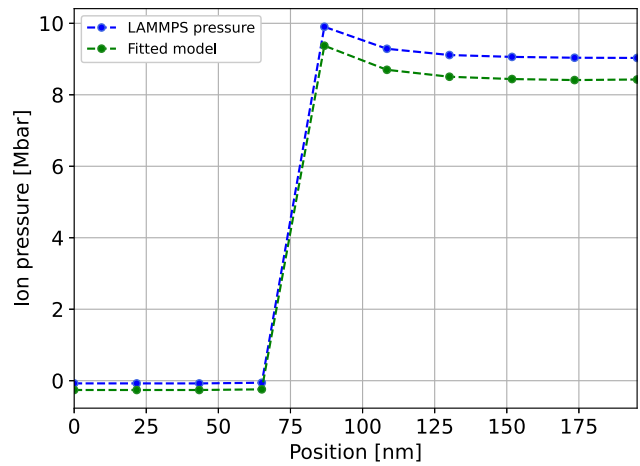


FIG. 7. The normalized proton excess pressure vs position for a WDM shock with $\Gamma_{i0} = 10$, $\theta_0 \approx 0.2$, and $M_{wc} = 5$. The LAMMPS pressure is from Yukawa-OCP simulations using the equivalent shock temperature and density values.

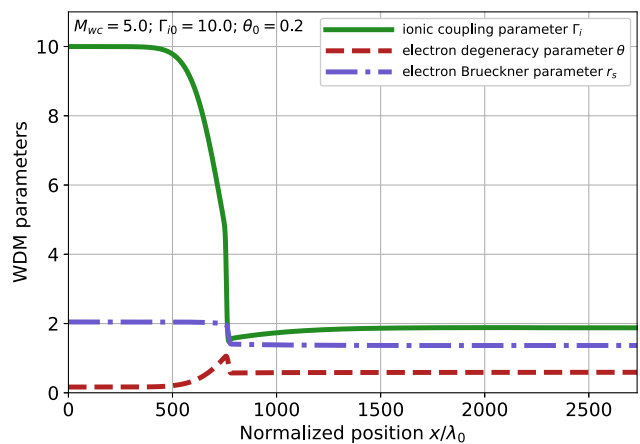


FIG. 8. Key WDM parameters vs position for a WDM shock with $\Gamma_{i0} = 10$, $\theta_0 \approx 0.2$, and $M_{wc} = 5$.

As mentioned before, our upstream parameter choices (Γ_{i0} , θ_0 , and M_{wc}) are a compromise between computational expediency, and relevance to WDM regimes of interest (e.g., ICF plasmas). Nonetheless, we need to address the impact of $r_s > 1$, which we consider in Sec. VIII.

VIII. ESTIMATING THE IMPACT OF ELECTRON NON-IDEALITY AND ION-ELECTRON CORRELATIONS

As mentioned previously, strong coupling effects in the electrons (i.e., non-ideality) and strong ion–electron correlations will alter the electron and ion EOS. This means that a simple post-processing of the excess electron pressure and the ion–electron pressure will not allow an apples-to-apples comparison to our results with ideal Fermi electrons since the downstream conditions could differ considerably between our original shock solution and the corrected one.

To overcome this problem, we appeal to the self-similarity of strong, steady-state, planar, plasma shocks in the non-degenerate/weakly coupled regime. Specifically, we note that—since the three principal regions within these shocks all scale $\propto \lambda_{ii}$ —all such shocks are the same length in the normalized coordinate, x/λ_{HH0}^{wc} . Similarly, although the scale factor is not necessarily known, the temperature, density, and pressure all scale by a factor which depends upon the shock Mach number, ion mass, charge state, and the upstream temperature/density. Hence, the properly normalized density and temperature will also look the same across Mach numbers for $M \gg 1$ (given the same upstream conditions).

Let us assume that WDM shocks also exhibit a self-similarity like this, but with respect to their EOS. More specifically, let us assume that a change in the electron and/or ion EOS amounts to scaling the gradients in the ion + electron densities and temperatures by some multiplier set by the corrected jump conditions. In other words,

$$Q_{\text{non-ideal}}(x) \equiv \chi_Q \int_0^x dx' \frac{dQ_{\text{ideal}}(x')}{dx'} + Q_{\text{ideal}}^0, \quad (51)$$

where “ideal” refers to the original quantities (as given by simulations using a Yukawa-OCF EOS for the ions, and an ideal Fermi EOS for the electrons), χ_Q is a scale factor; Q can be the electron temperature, ion temperature, or the mass density. By choosing to scale the gradients, we can force $Q_{\text{non-ideal}}(x \rightarrow \infty) = Q_{\text{non-ideal}}^0$, and $Q_{\text{non-ideal}}(x \rightarrow -\infty) = Q_{\text{ideal}}(x \rightarrow -\infty) = Q_{\text{ideal}}^0$ —i.e., despite the two solutions differing in scale, they will have the same upstream temperatures and densities.

To proceed, we require expressions for the electron excess pressure and the proton–electron pressure. To that end, we appeal to the Chabrier and Potekhin⁴¹ fit for the proton–electron excess (Helmholtz) free energy given a hydrogen plasma; i.e., their Eq. (29). This fit, which accounts for mild relativistic effects in the electrons, is good to a few percentage points across a wide range of Γ_i and r_s . Given f_{ie} —the proton–electron excess free energy—the proton–electron pressure, p_{ie} can be calculated from the thermodynamic relation⁴¹

$$\frac{p_{ie}}{n_i T} \equiv \frac{1}{3} \left[\left(\frac{\partial f_{ie}}{\partial \ln \Gamma} \right)_{r_s} - \left(\frac{\partial f_{ie}}{\partial \ln r_s} \right)_{\Gamma} \right], \quad (52)$$

where Γ and T remain ambiguous, in our case. Whereas Chabrier and Potekhin⁴¹ assume that $T_i = T_e \equiv T$ —so that, $\Gamma_i = \Gamma_e \equiv \Gamma$ —we allow $T_i \neq T_e$. Hence, it is unclear if the Chabrier and Potekhin⁴¹ fit strictly applies to our shock problem. Nonetheless, since T_i and T_e only ever differ from each other by a factor of a few (~ 2) within the shock front, we believe that the Chabrier and Potekhin⁴¹ fit is likely still accurate enough for our purposes. With this in mind, we take $\Gamma = \Gamma_e \equiv e^2/(aT_e)$ and $T = T_i$.

Next, to calculate the electron excess pressure, we employ the Ichimaru, Iyetomi, and Tanaka (IIT)⁴² fit. This fit to the electron excess free energy, f_{ee}^{ex} —or, in the parlance of density functional theory, the correlation–exchange free energy—is also very accurate. In this case, the excess pressure is given by⁴²

$$\frac{p_e^{ex}}{n_e T} \equiv \frac{1}{3} \left\{ \left[\frac{E_{\text{int}}}{NT} \right] - 2 \left(\frac{\partial f_{ee}^{ex}}{\partial \ln \theta} \right)_{\Gamma} \right\}, \quad (53)$$

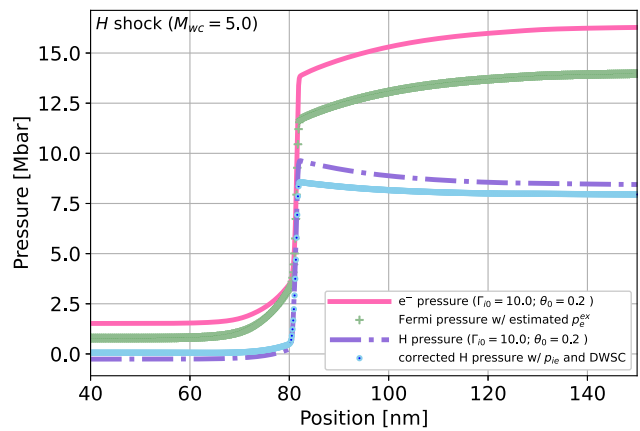
where the first term on the RHS is the interaction energy (for which, IIT also provide an accurate fit). As before, $T_e = T_i \equiv T$ is assumed in the IIT derivation. We opt to take $T = T_e$ and $\Gamma = \Gamma_e$.

Finally, we show plots of the re-normalized shock electron + proton pressures in Fig. 9(a), and Fig. 9(b) shows the total pressure. Here, we take the new proton pressure to be $p_i = (1 + \alpha_{\text{DWSC}})n_i T_i + p_{ie}$ so that we can account for the partial proton–electron correlation contribution provided by α_{fit} .

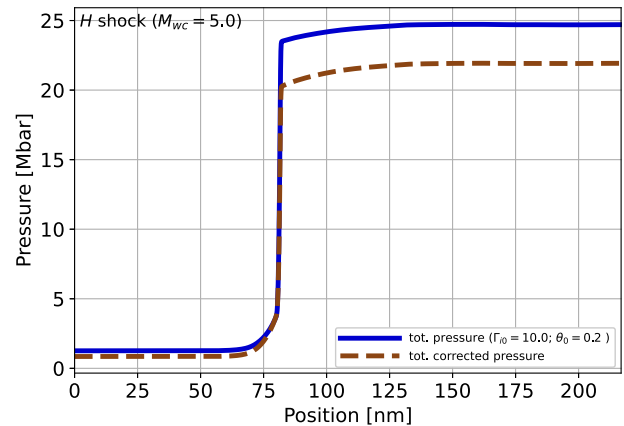
Interestingly, the ideal and non-ideal—as defined by Eq. (51)—proton pressures are very similar in Fig. 9(a), indicating that the Virial theorem applied to a Yukawa-OCF does a decent job of emulating the proton–electron contribution to the EOS—at least, for $r_s \sim 2$. As promised, the renormalized proton pressure is greater than zero everywhere, including the upstream region.

Unfortunately, the ideal and non-ideal—as defined by Eq. (51)—electron pressures are more notably different in Fig. 9(a); p_e^{ex} is just not negligible at these conditions.

Despite the differences, we are encouraged by the fact that the two shock solutions have the same qualitative shape, suggesting that



(a) The proton and electron pressures.



(b) The total plasma pressure.

FIG. 9. Renormalized pressure profiles for the WDM shock with $\Gamma_{i0} = 10$, $\theta_0 \approx 0.2$, and $M_{wc} = 5$. Here, we include the post-processed electron and proton pressures which account for the proton–electron contribution to the proton Virial and the electron excess pressure.

our assumption of self-similarity does, in fact, hold. Furthermore, the original total pressure—as shown in Fig. 9(b)—is fairly close to the renormalized one, where the principal differences are downstream of the shock ($\sim 10\%$). Thus, although our shock solution effectively uses the wrong boundary conditions (i.e., the shock jump conditions are in error), this does not appear to affect the qualitative features of the shock solution.

In Sec. IX, we consider a final source of error: kinetic effects.

IX. ASSESSING KINETIC EFFECTS

In weakly coupled steady-state systems composed of classical particles, the validity of the equations of hydrodynamics depends upon the Knudsen number, N_K —which is the ratio of a characteristic spatial gradient scale to the particles' mean-free-path. The reason for this is that the fluid transport coefficients—which are essential to close the system of hydrodynamic equations—are derived under the assumption of local thermal equilibrium (LTE). As a rule of thumb, non-LTE (i.e., kinetic) effects appear at $N_K \geq 10^{-3}$ for plasmas.

Figure 10(a) shows the (kinetic pressure, nT) Knudsen numbers for the non-degenerate, weakly coupled protons and electrons from our Mach 5 plasma shock simulation. Note that both the proton and electron Knudsen numbers are well above 10^{-3} inside the shock. This impacts the transport of energy and momentum within the shock, leading to a very different shock structure when kinetic effects are accounted for by simulating the shock using a kinetic code.^{6–8,10}

To assess ion kinetic effects within a WDM shock, we use the generalized Bannasch mfp³⁷ to define a Bannasch–Knudsen number, $N_{KB} \equiv \lambda_B \nabla \ln Q$ —where Q is some hydrodynamic quantity and $\lambda_B \equiv v_{th} \tau_B$ is the Bannasch generalized mfp.

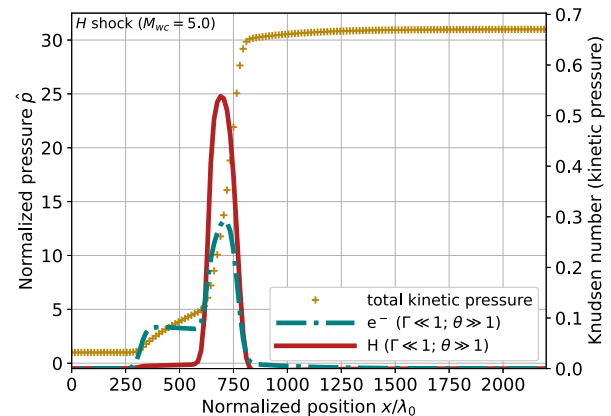
Figure 10(b) shows the proton Bannasch–Knudsen numbers, N_{KB} across our WDM shock ($M_{wc} = 5$; $\theta_0 \approx 0.2$; $\Gamma_{i0} = 10$). Here, the gradient scale is taken from the kinetic pressure, $n_i T_i$ [as done in Fig. 10(a)]. Unsurprisingly, N_{KB} approaches similar values to non-degenerate/weakly coupled equivalent in the vicinity of the ion compression shock. On the whole, the qualitative features are largely the same between Figs. 10(a) and 10(b).

We also show an estimate for the electron Knudsen number in Fig. 10(b). Here, we define the effective mfp as $v_{the} \tau_F$. In this respect, the Knudsen number, $N_K^{ei} \equiv v_{the} \tau_F \times [\partial_x \log(n_e T_e)]$ tells us something about the kinetic effects associated with the electron–proton collisions. We observe that N_K^{ei} remains large throughout the electron pre-heat layer of both shocks, indicating that kinetic effects will impact the electron heat flux there. The total impact, however, is hard to predict since the various drivers of energy and momentum transport within the shock can counter each other, leading to only a modest overall change in the shock structure—as recent results for the full kinetic structure of a non-degenerate/weakly coupled plasma shock show.¹⁰

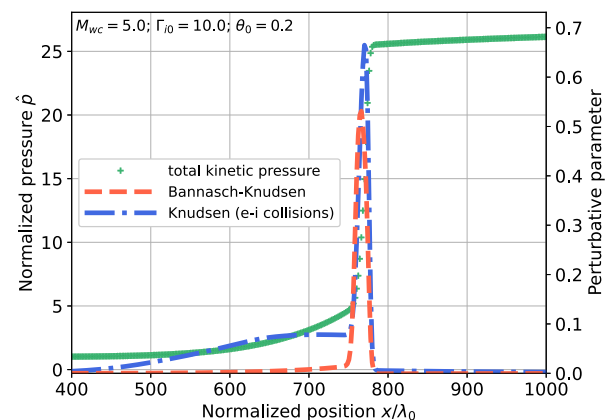
Finally, we point out that non-local EOS effects²⁴ will also be more pronounced at these strong gradient sites. A self-consistent quantification of both kinetic and non-local correlation effects on shock structure requires a first-principle treatment appealing to a generalized kinetic equation.

X. CONCLUSIONS

In this work, we simulated a strong, steady-state, planar WDM shock in hydrogen plasma using the single-purpose fluid code, *SHion*. In this context, WDM refers to a plasma characterized by strongly



(a) The proton and electron Knudsen numbers vs. position for an $M_{wc} = 5$ with non-degenerate, weakly-coupled electrons+protons. Also plotted is the total kinetic pressure, $n_e T_e + n_i T_i$.



(b) The Bannasch–Knudsen number (protons), the degenerate Knudsen number (electrons), and the total kinetic pressure vs. position for a WDM shock ($\Gamma_{i0} = 10$, $\theta_0 \approx 0.2$, and $M_{wc} = 5$).

FIG. 10. Perturbative parameters evaluated within the WDM and non-degenerate/weakly coupled $M_{wc} = 5$ shocks. For a non-degenerate/weakly coupled plasma, the proton Knudsen number determines the validity of the fluid approximation; with hydro models breaking down for $N_K \geq 10^{-3}$. For WDM shocks, we define an analogous parameter—the Bannasch–Knudsen number—which properly accounts for the proton–proton collisional relaxation time, given $\Gamma_i > 1$. As done in Fig. 5(a), the abscissas for both plots is normalized to the upstream mean-free-path, as defined by Eq. (50).

coupled ions + fully Fermi degenerate electrons. We found that—unlike the classical, weakly coupled ions + electrons analogue; whose structure depends solely on the Mach number—a strong WDM shock (for a planar geometry in steady state) also depends upon the upstream electron degeneracy parameter, $\theta_0 = T_0/T_{F0}$, and the ionic Coulomb coupling parameter, $\Gamma_{i0} = e^2/(aT_0)$.

We find that our simulated WDM shock ($M_{wc} = 5$; $\theta_0 \approx 0.2$; $\Gamma_{i0} = 10$) differs in some ways from the non-degenerate/weakly coupled counterpart in the detailed structure. Namely, when compared to the appropriate upstream ion–ion mean-free-path (mfp), the electron

pre-heat layer is much shorter in the WDM shock than it is in the non-degenerate/weakly coupled equivalent. However, the mfp normalized thermalization layers have nearly the same length between the two solutions—suggesting that the WDM thermalization layer length has the same scaling with the mfp and ion/electron mass ratio as the non-degenerate/weakly coupled one. Whether or not this is unique to a hydrogen (proton) plasma, or if it applies generally throughout the WDM regime, is yet to be determined.

In Sec. VIII, we considered what impact EOS errors could have on our shock solution. Namely, we estimate the excess pressure contribution to the degenerate electron EOS, and the contribution of proton–electron correlations to the proton EOS. We find that, although these effects may meaningfully affect the shock jump conditions in a real system, the overall impact on the shock structure appears minimal.

Additionally, we showed in Sec. IX that ion and electron kinetic effects are likely just as important for strong WDM shocks as they are for non-degenerate/weakly coupled ones. This is contrary to the expectation offered by effective potential theory models for OCP transport coefficients, which show⁴³ that 2nd-order corrections to the Chapman–Enskog derived transport coefficients approach zero for $\Gamma \gg 1$. Since these corrections represent higher-order deviations from local thermal equilibrium, their suppression at strong coupling suggests a weakening of kinetic effects. However, this undoubtedly has its limits in systems with strong spatial inhomogeneity—as is the case for strong shocks.

It is worth mentioning that the structure of a plasma shock, in general, may be consequential. This is because, although the length of a shock is typically smaller than the system size of interest (e.g., in an ICF capsule), shocks can leave imprints behind when they reflect off boundaries⁴⁴ or breakout of material interfaces.^{45,46} These imprints are transient but sometimes result in long-lasting ion species density stratification or temperature separation. Of course, this effect will only occur in a plasma mixture, but the vast majority of plasma settings have multiple ion species. While it is clear that these imprinting effects may be important in weakly coupled plasmas, we do not know what to expect at strong-coupling since non-local EOS and non-ideal transport effects may contribute in unanticipated ways.

On a related note, differences in pressure profiles compared to non-degenerate/weakly coupled shocks could significantly affect the hydrodynamic instability development in the context of ICF, by changing the vorticity deposition at material interfaces.

Finally, we note that the most faithful treatment of a WDM shock requires a fully quantum kinetic treatment. This would be a heroic calculation since something akin to an expensive path integral Monte Carlo, density functional theory, or non-equilibrium quantum molecular dynamics simulation would be required. Nonetheless, until such a simulation is completed, the full self-consistent structure of a WDM shock will remain unknown.

ACKNOWLEDGMENTS

We thank Abdou Diaw for helpful discussions and for providing us with a basic LAMMPS deck. We also thank David Stark for giving us the idea of scaling the temperatures and densities in our excess pressure comparisons. Work performed under the auspices of the U.S. Department of Energy National Nuclear Security Administration under Contract No. 89233218CNA000001 and used resources provided by

the Los Alamos National Laboratory Institutional Computing Program. This work was partially supported by the Laboratory Directed Research and Development program of Los Alamos National Laboratory under Project No. 20190005DR (all authors) and the Consortium for Nuclear Security Technologies (CONNECT) NNSA Minority Serving Institution Partnership Program (MSIPP) under Contract No. DE-NA0003948 (CDS).

AUTHOR DECLARATIONS

Conflict of Interest

The authors have no conflicts to disclose.

Author Contributions

Brett Dale Keenan: Conceptualization (lead); Data curation (lead); Formal analysis (equal); Funding acquisition (supporting); Investigation (lead); Methodology (lead); Project administration (lead); Resources (supporting); Software (supporting); Supervision (equal); Validation (lead); Visualization (lead); Writing – original draft (lead); Writing – review & editing (lead). **Chrismond Smith:** Conceptualization (supporting); Data curation (supporting); Formal analysis (supporting); Investigation (supporting); Resources (supporting); Software (supporting); Visualization (supporting); Writing – review & editing (supporting). **Daniel Livescu:** Conceptualization (supporting); Funding acquisition (equal); Investigation (supporting); Methodology (supporting); Project administration (supporting); Resources (supporting); Supervision (supporting); Writing – review & editing (supporting). **Jeffrey R. Haack:** Conceptualization (supporting); Funding acquisition (supporting); Methodology (supporting); Project administration (supporting); Supervision (supporting); Writing – review & editing (supporting). **Robert S. Pavel:** Methodology (supporting); Software (supporting).

DATA AVAILABILITY

The data that support the findings of this study may be obtained from the corresponding author upon reasonable request.

REFERENCES

- ¹M. Bonitz, T. Dornheim, Z. A. Moldabekov, S. Zhang, P. Hamann, H. Kählert, A. Filinov, K. Ramakrishna, and J. Vorberger, *Phys. Plasmas* **27**, 042710 (2020).
- ²J. D. Jukes, *J. Fluid Mech.* **3**, 275 (1957).
- ³V. D. Shafranov, *Sov. Phys. JETP* **5**, 1183 (1957).
- ⁴M. Y. Jaffrin and R. F. Probst, *Phys. Fluids* **7**, 1658 (1964).
- ⁵M. S. Grewal, *Phys. Fluids* **16**, 561 (1973).
- ⁶M. Casanova, O. Larroche, and J. P. Matte, *Phys. Rev. Lett.* **67**, 2143 (1991).
- ⁷F. Vidal, J. P. Matte, M. Casanova, and O. Larroche, *Phys. Fluids B* **5**, 3182 (1993).
- ⁸B. D. Keenan, A. N. Simakov, L. Chacón, and W. T. Taitano, *Phys. Rev. E* **96**, 053203 (2017).
- ⁹Z. Li and D. Livescu, *Phys. Plasmas* **26**, 012109 (2019).
- ¹⁰S. E. Anderson, L. Chacón, W. T. Taitano, A. N. Simakov, and B. D. Keenan, *Phys. Rev. E* **104**, 055205 (2021).
- ¹¹M. S. Green, *J. Chem. Phys.* **22**, 398 (1954).
- ¹²R. Kubo, *J. Phys. Soc. Jpn.* **12**, 570–586 (1957).
- ¹³J. P. Hansen and I. R. McDonald, *Phys. Rev. A* **23**, 2041 (1981).
- ¹⁴M. Gell-Mann and K. A. Brueckner, *Phys. Rev.* **106**, 364 (1957).
- ¹⁵J. M. Ziman, *Philos. Mag.* **6**, 1013 (1961).
- ¹⁶H. Minoo and C. Deutsch, *Phys. Rev. A* **14**, 840 (1976).

- ¹⁷H. G. Rinderknecht, P. A. Amendt, S. C. Wilks, and G. Collins, *Plasma Phys. Controlled Fusion* **60**, 064001 (2018).
- ¹⁸B. Tummers, see <https://datathief.org/> “DataThief III” (2006).
- ¹⁹A. Diaw, K. Barros, J. Haack, C. Junghans, B. Keenan, Y. W. Li, D. Livescu, N. Lubbers, M. McKerns, R. S. Pavel, D. Rosenberger, I. Sagert, and T. C. Germann, *Phys. Rev. E* **102**, 023310 (2020).
- ²⁰G. Dimonte and J. Daligault, *Phys. Rev. Lett.* **101**, 135001 (2008).
- ²¹A. N. Simakov, B. D. Keenan, W. T. Taitano, and L. Chacón, *Phys. Plasmas* **24**, 092702 (2017).
- ²²S. I. Braginskii, in *Reviews of Plasma Physics*, edited by M. A. Leontovich (Consultants Bureau, New York, 1965), Vol. 1, p. 205.
- ²³J. H. Irving and J. G. Kirkwood, *J. Chem. Phys.* **18**, 817 (1950).
- ²⁴A. Diaw and M. S. Murillo, *Phys. Rev. E* **99**, 063207 (2019).
- ²⁵M. Baus and J.-P. Hansen, “Statistical mechanics of simple coulomb systems,” *Phys. Rep.* **59**(1), 1 (1980).
- ²⁶P. Vieillefosse and J. P. Hansen, *Phys. Rev. A* **12**, 1106 (1975).
- ²⁷B. Scheiner and S. D. Baalrud, *Phys. Rev. E* **102**, 063202 (2020).
- ²⁸L. G. Stanton and M. S. Murillo, *Phys. Rev. E* **93**, 043203 (2016).
- ²⁹K. Huang, *Statistical Mechanics*, 2nd ed. (John Wiley & Sons, Inc., 1991), pp. 187–188.
- ³⁰Y. T. Lee and R. M. More, *Phys. Fluids* **27**, 1273 (1984).
- ³¹D. Bennaceur and A. H. Khalfaoui, *Phys. Rev. E* **48**, 2111 (1993).
- ³²G. Dimonte, *Phys. Plasmas* **27**, 052709 (2020).
- ³³R. Zimmermann, *Many Particle Theory of Highly Excited Semiconductors* (Teubner, Leipzig, 1988).
- ³⁴X. Aymerich-Humet, F. Serra-Mestres, and J. Millán, *J. Appl. Phys.* **54**, 2850 (1983).
- ³⁵S. Plimpton, *J. Comput. Phys.* **117**, 1 (1995).
- ³⁶H. DeWitt, W. Slattery, and G. Chabrier, *Physica B* **228**, 158 (1996).
- ³⁷G. Bannasch, J. Castro, P. McQuillen, T. Pohl, and T. C. Killian, *Phys. Rev. Lett.* **109**, 185008 (2012).
- ³⁸B. D. Keenan, A. N. Simakov, W. T. Taitano, and L. Chacón, *Phys. Plasmas* **25**, 032103 (2018).
- ³⁹B. D. Keenan, W. T. Taitano, and K. Molvig, *Phys. Plasmas* **27**, 042704 (2020).
- ⁴⁰M. Navet, E. Jamin, and M. R. Feix, “Virial’ pressure of the classical one-component plasma,” *J. Phys. Lett.* **41**(3), 69–73 (1980).
- ⁴¹G. Chabrier and A. Y. Potekhin, *Phys. Rev. E* **58**, 4 (1998).
- ⁴²S. Ichimaru, H. Iyetomi, and S. Tanaka, *Phys. Rep.* **149**, 91 (1987).
- ⁴³B. Scheiner and S. D. Baalrud, *Phys. Rev. E* **100**, 043206 (2019).
- ⁴⁴W. T. Taitano, L. Chacón, and A. N. Simakov, *J. Comput. Phys.* **365**, 173 (2018).
- ⁴⁵C. Bellei and P. A. Amendt, *Phys. Plasmas* **24**, 040703 (2017).
- ⁴⁶B. D. Keenan, W. T. Taitano, A. N. Simakov, L. Chacón, and B. J. Albright, *Phys. Plasmas* **27**, 022704 (2020).